# *In Situ* Calorimetry Study on Cooling of the Metallic-Glass Forming Melts

Xin-Yu Luo(罗新宇)[1,2], Qi Cheng(程琪)[3*], Yong-Hao Sun(孙永昊)[1,2*], and Wei-Hua Wang(汪卫华)[1,2,4]

[1]*Institute of Physics, Chinese Academy of Sciences, Beijing 100190, China*
[2]*School of Physical Sciences, University of Chinese Academy of Sciences, Beijing 100049, China*
[3]*School of Physics and Electronic Information, Anhui Normal University, Wuhu 241000, China*
[4]*Songshan Lake Materials Lab, Dongguan 523808, China*

(Received 29 October 2025; accepted manuscript online 25 November 2025)

Optimizing the microchannel design of the next generation of chips requires an understanding of the *in situ* property evolution of the chip-based materials under fast cooling. This work overcomes the conventional reliance on reheating data of melt-quenched glasses by demonstrating direct observations of glass transition on cooling curves utilizing the most advanced fast differential scanning calorimetry. By leveraging an MEMS chip sensor that allows for rapid heat extraction from microgram-sized samples to a purged gas coolant, the device is able to reach ultra-fast cooling rates of up to 40,000 $\mathrm{K{\cdot}s^{-1}}$. Four thermal regions are identified by examining the cooling behaviors of two metallic glasses. This is because the actual rate of the specimen can differ from the programmed rate, especially at high set rate when the actual rate decreases before the glass transition is completed. We define the operational window for reliable cooling curve analysis, build models with empirical and theoretical analyses to determine the maximum feasible cooling rate, and demonstrate how optimizing sample mass and environment temperature broaden this window. The method avoids deceptive structural relaxation effects verified by fictive-temperature analysis and permits the capture of full glass transition during cooling.

DOI: 10.1088/0256-307X/43/1/010603 CSTR: 32039.14.0256-307X.43.1.010603

Heat-flux density in a single silicon-based chip now exceeds 1 $\mathrm{kW{\cdot}cm^{-2}}$ due to the rapid advancements in artificial intelligence, high-performance computing, and 5G communication, placing unprecedented demands on thermal management. The embedded cooling approach is essential for controlling rapidly increasing heat fluxes because it incorporates the cooling solution directly onto or within the active electronic components and removes thermal resistances present in conventional separable heat sinks. A thorough understanding of fast cooling, including both microchannel design and the structural change involved in chip materials, is required for high-standard thermal management.[1] Fortunately, the most advanced fast differential scanning calorimetry (FDSC) rises to the challenge. Commercialized by Mettler-Toledo company, it allows for the *in-situ* observation of heat flow under controlled high cooling rates. The device utilizes an MEMS chip sensor and investigates micro- or nano-gram scale specimens in programmable thermal profiles with heating rates ($\phi_\mathrm{h}$) ranging from 0.1 to 60,000 $\mathrm{K{\cdot}s^{-1}}$ [40,000 $\mathrm{K{\cdot}s^{-1}}$ at maximum for cooling rate ($\phi_\mathrm{c}$)].[2]

Many alloy melts can be vitrified *in situ* thanks to the advanced FDSC, which makes it possible to repeat the melt-quenching procedures on a single specimen. This is appealing because a $\phi_\mathrm{c}$ of no more than 5 $\mathrm{K{\cdot}s^{-1}}$ can be obtained using conventional differential scanning calorimetry. One example is the formation of metallic glass (MG), which is achieved by melt quenching at high $\phi_\mathrm{c}$. Their long-range disordered and short-range ordered structure enables excellent mechanical properties like high yield strength, high resilience, and in some cases high fracture toughness,[3] as well as outstanding soft-magnetic properties of the Fe-based MGs.[4] These properties make them suitable for applications in aerospace, automotive industries, and high-precision engineering.[5–7] In manufacturing, fast cooling is typically achieved by suction casting,[8] melt spinning,[9] and physical vapor deposition,[10] as required for suppressing crystallization and promoting glass formation. *In situ* cooling while monitoring the diffraction pattern and viscosity of electrostatically elevated MG balls has been demonstrated during slow cooling, from which recalescence resembling crystallization can be detected.[11] However, fast cooling in production functions like a black box with little knowledge about the temperature, structure, and viscosity changes of the melt during rapid quenching.

Luo *et al.* summarize the application of FDSC for investigating polymeric and molecular glasses, covering sample preparation, thermal-lag correction, crystallization dynamics, liquid–liquid transitions, and glass stability, with implications for MG research.[2] Zhang *et al.* reveal that the glass-transition temperature of hybrid glasses is size-independent at micrometer scales, despite their glass-transition enthalpy exhibiting a clear size dependence.[12] Liu *et al.* utilize FDSC to measure the viscosity of metallic supercooled liquids over a wide range

*Corresponding authors. Email: chengqi@ahnu.edu.cn; ysun58@iphy.ac.cn
© 2026 Chinese Physical Society and IOP Publishing Ltd. All rights, including for text and data mining, AI training, and similar technologies, are reserved.

and define an optimal processing window for thermoplastic forming.[13] Shen *et al.* provide direct evidence of a first-order liquid–liquid transition above,[14] around,[15] and below[16] the glass-transition temperature in MGs, revealing both nucleation-growth and spinodal-decomposition transition mechanisms.[15] Cheng *et al.* demonstrate that FDSC can be used not only for thermal analysis of MGs but also as an engineering tool[17] to design different types of glasses[18] and crystals,[19] to distinguish phase transitions in melts,[20,21] and to optimize glass-forming ability.[22,23]

Despite these efforts, it seems that the glass transition has rarely been investigated on the cooling curves. Glass transition in cooling just reflects the effect of melt quenching, in contrast to glass transition in heating, which reflects the combined effects of liquid quenching and structural relaxation of glass. Conventional DSC cannot accomplish this, but FDSC can. Instead of looking directly at the cooling curves, people are more inclined to look at the reheating curves and infer the $\phi_c$ effects on the specimen. Undeniably, it can be said that the FDSC cooling curves contain features that differ from or are absent in the heating curves and call for detailed explanation.[24,25] This is exactly the aim of the present paper. We show that there are thermal ranges where the sample $\phi_c$ is less than set values, rendering deceptive findings. We also demonstrate that the operating window of fast cooling may be expanded by optimizing sample mass and environmental temperature, enabling people to capture a full glass transition during fast cooling.

Two MGs were studied, including $Pd_{35}Ni_{45}P_{20}$ and $Au_{42.3}Ag_{5.6}Pd_{2.4}Cu_{27.5}Si_{22.2}$ (in atomic percentages hereafter). Selection of the MG compositions was performed on the robotic AI-Scientist platform of the Chinese Academy of Sciences. The Pd-Ni alloy ingots were prepared by arc-melting mixtures of Pd (99.99% purity) and Ni (99.99% purity) in an Ar atmosphere purified with a Ti getter. The Pd-Ni alloy ingots were then melted with P (99.5% purity) by induction melting in an Ar environment to create the master alloy, which was then fluxed in $B_2O_3$ at 1000 ℃ for 10 h. The ribbons were finally made by melt spinning onto a copper wheel in an Ar atmosphere at a tangential velocity of about 60 $m{\cdot}s^{-1}$, and the ribbon thickness is about 20 μm, following the procedure of Ref. [26]. Details of $Au_{42.3}Ag_{5.6}Pd_{2.4}Cu_{27.5}Si_{22.2}$ metallic-glass preparation are provided in Ref. [18].

Specimens used for FDSC were prepared using a Leica IC90E optical microscope with 120× magnification. The ribbon was cut into μm-size pieces using a stainless-steel scalpel, and one piece was attached to a thin hair with electrostatic force and then transferred to the center of sensor. The sample mass ($m$) was calculated by comparing the melting enthalpy obtained from the heating curves of FDSC with that measured in differential scanning calorimetry (DSC 8500, Perkin-Elmer) at a heating rate ($\phi_h$) of 20 $K{\cdot}min^{-1}$. Figure 1(a) presents the experimental set-ups in the FDSC chamber. Normally, the melt-quenched FDSC specimens would not have a shape of pudding but appear like a ball or a hill. However, the sketched geometry can simplify the heat-transfer calculation into one dimension, which is useful for thermal-profile estimation. For the specimen, the bottom surface is hot as it is attached to the sensor beneath which are thermocouples and heaters; the top surface is cold as it is surrounded by flowing gas coolant with a pre-set environment temperature ($T_e$). Thus, the sensor temperature ($T_{sen}$), i.e., the sample temperature as characterized, measures at the specimen bottom, and a thermal gradient exists from bottom to top surfaces. Schawe *et al.*[24] suggested that the temperature difference between the bottom and upper surfaces ($\Delta T_s$) is

$$\Delta T_s = \frac{T_{sen} - T_e}{1 + \frac{\lambda}{\kappa H}}, \tag{1}$$

where $\lambda$ and $\kappa$ are thermal conductivity of the material and heat-transfer coefficient between the material and gas, respectively. $H$ is the specimen thickness. Equation (1) points out that larger $\lambda$, smaller $\kappa$, and smaller $H$ are preferable for a negligible $\Delta T_s$ (indicating no thermal gradient in the specimen). That is why metals (high $\lambda$), gas coolant (low $\kappa$), and thin specimens are preferable for FDSC experiments. Additionally, equation (1) considers the steady-state condition for heat transfer, in which the specimen temperature at the top surface is always smaller than that at the bottom ($T_{sen}$). This is valid only when the non-equilibrium instantaneous thermal transfer or the characteristic time ($\tau$) for the top surface to encounter a temperature rise can be neglected. It follows

$$\tau = \frac{H^2}{2D}, \tag{2}$$

where $D$ is the thermal diffusivity of the material. For MGs, $D$ is around (2–4) $\times 10^{-6}$ $m^2{\cdot}s^{-1}$,[27] so for a 1 μm-thick specimen, $\tau$ is only 125–250 ns. The time resolution of the Mettler-Toledo FDSC 2+ is at best 1 ms, largely exceeding the $\tau$ we have estimated, indicating that data is always acquired from the specimen staying at a steady-state thermal profile [Fig. 1(a)]. Thus, the specimen can be near-uniformly (low $\Delta T_s$) heated from the bottom, even if it is immersed in an environment of gas coolant. Although using gas (low $\kappa$) instead of liquid (high $\kappa$) as coolant reduces the maximum $\phi_c$ we can apply, it allows low $\Delta T_s$ or less thermal gradient in the metallic specimens.

In this work, the MG specimens were studied using a high-temperature UFH sensor (maximum operating at 1000 ℃). During the test, the sample chamber was continuously purged with high-purity argon at a flow rate of 100 $ml{\cdot}min^{-1}$. To ensure that the specimens were properly adhered to the sensor before the test, each specimen was heated to 50 K or 335 K above its melting temperature ($T_m$), quenched back to $T_e$, and repeated three times with the same procedure. All the materials were heated from $T_e$ to a quenching temperature ($T_q$) at a $\phi_h$, held for a duration ($t_{hold}$) at $T_q$, and then cooled back to $T_e$ at a $\phi_c$ ranging from 10 to 40,000 $K{\cdot}s^{-1}$. Guidelines for the thermal protocol are provided in Fig. 1(b). Table 1 lists all the parameters obtained from literature and experiments using the investigated MGs.

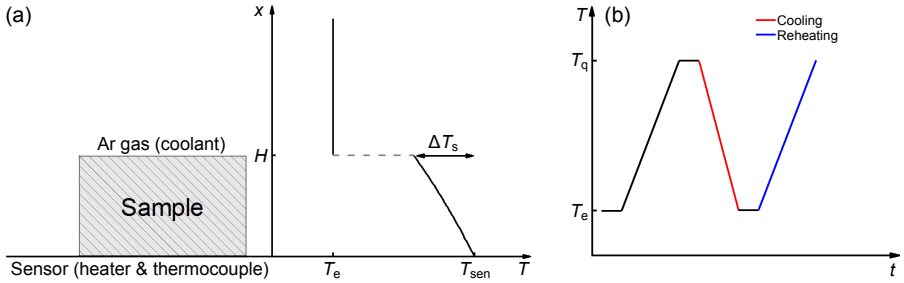


**Fig. 1.** Fast-cooling geometry and program. (a) Experimental set-ups, and the corresponding temperature ($T$) profile in height direction ($x$). $H$, the sample thickness; $T_{\rm sen}$, sensor temperature; $T_{\rm e}$, environment temperature; $\Delta T_{\rm s}$, temperature variation between the top and bottom surfaces of the specimen. (b) Thermal protocols applied in this study. $t$, time; $T_{\rm q}$, quenching temperature.

**Table 1.** Materials properties and thermal-protocol set-ups. $\lambda$, thermal conductivity; $\kappa$, heat-transfer coefficient (in forced convection of gas purging); $m$, sample mass; $T_{\rm m}$, melting temperature; $T_{\rm e}$, environment temperature; $t_{\rm hold}$, holding duration; $\phi_{\rm h}$, heating rate.

| Materials | $\lambda$ ($\rm W{\cdot}m^{-1}{\cdot}K^{-1}$) | $\kappa$ ($\rm W{\cdot}m^{-1}{\cdot}K^{-1}$) | $m$ (ng) | $T_{\rm m}$ (K) | $T_{\rm q}$ (K) | $T_{\rm e}$ (K) | $t_{\rm hold}$ (s) | $\phi_{\rm h}$ ($\rm K{\cdot}s^{-1}$) |
|---|---|---|---|---|---|---|---|---|
| Pd-based | ∼7 [27] | ∼100 | 230 | 973 | 1,023 | 183 | 0.1 | 2,000 |
| Au-based | ∼10 [28] | ∼100 | 290/420 | 638 | 973 | 300/223 | 0.1 | 500 |

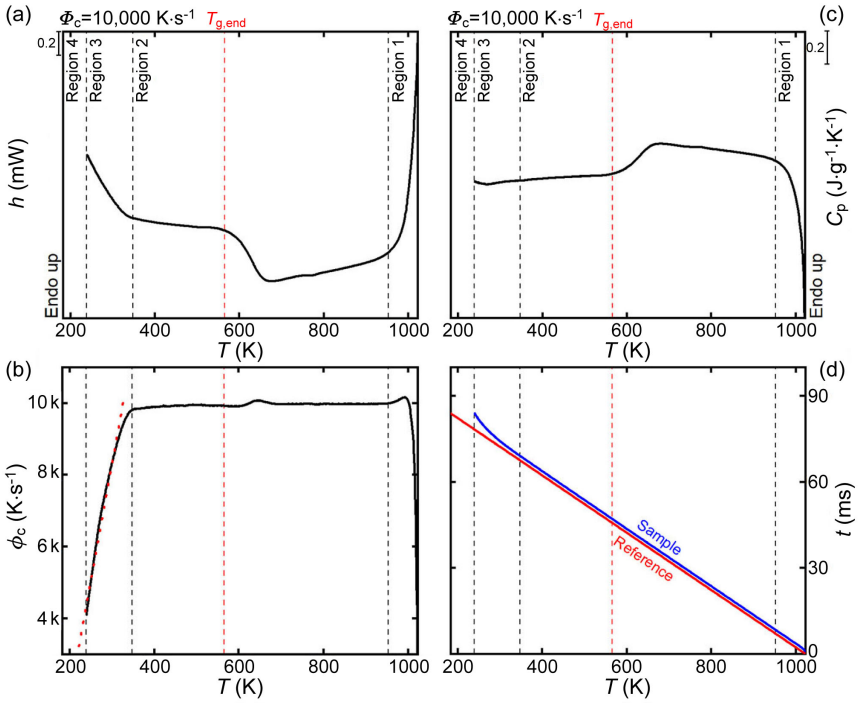


**Fig. 2.** Melt quenching of $Pd_{35}Ni_{45}P_{20}$ at a set cooling rate $\Phi_{\rm c}$ of 10,000 $\rm K{\cdot}s^{-1}$. (a) The heat flow $h$ cooling trace. $T_{\rm g,end}$ refers to the ending temperature of glass transition in cooling (as indicated by the red-dashed line). Regions 1–4 are separated by the black-dashed lines. (b) The cooling rate $\phi_{\rm c}$ plotted against temperature $T$. The red-dotted line indicates a linear fit assuming Newtonian cooling. (c) The specific heat capacity $C_{\rm p}$ cooling trace. (d) Time of testing $t$. The sample and reference temperatures are indicated by blue and red curves.

Figure 2(a) presents a typical cooling curve of the $Pd_{35}Ni_{45}P_{20}$ melt at a $\phi_{\rm c}$ of 10,000 $\rm K{\cdot}s^{-1}$, where $h$ and $T$ stand for heat flow and temperature, respectively. We can distinguish four regions out of it. The definition depends on the correlation between $\phi_{\rm c}$ and the programmed cooling-rate $\Phi_{\rm c}$. Region 1 marks the beginning of cooling, where $h$ drops with the decreasing $T$. This behavior reflects the machine's response to the switch from isothermal holding to fast cooling. As shown in Fig. 2(b), there is a period for the actual $\phi_{\rm c}$ to catch up with $\Phi_{\rm c}$ of 10,000 $\rm K{\cdot}s^{-1}$ ($\phi_{\rm c} < \Phi_{\rm c}$). An overshoot ($\phi_{\rm c} > \Phi_{\rm c}$) is detected in Fig. 2(b) before stabilizing to $\Phi_{\rm c}$. Finally when $\phi_{\rm c} = \Phi_{\rm c}$, Region 1 ends and enters Region 2. Because $\phi_{\rm c} = \Phi_{\rm c}$, the cooling curve reflects the actual change in $h$ of the material at the given $\Phi_{\rm c}$, indicating effects of fast cooling. An obvious signal is an $h$-step that climbs up towards the exother-

mic direction with decreasing $T$ [Fig. 2(a)]. On the heating curves, an $h$-step representing glass transition climbs up towards the endothermic direction with increasing $T$, which is opposite to our observation. However, this is typical for the cooling curves, because when calculating the specific-heat capacity ($C_\mathrm{p}$) using

$$C_\mathrm{p} = \frac{h}{m\phi_\mathrm{c}}. \tag{3}$$

The minus sign of $\phi_\mathrm{c}$ needs to be included if $h$ is taken from cooling. This results in Fig. 2(c), where the $C_\mathrm{p}$ step of the glass transition in cooling points in the same direction as that in heating. In Fig. 2(a), fast cooling at a $\Phi_\mathrm{c}$ of 10,000 K·s$^{-1}$ stops at 347 K, causing both $C_\mathrm{p}$ and $\phi_\mathrm{c}$ to drop with decreasing $T$. This marks Region 3, where the power is switched off, allowing the specimen to be naturally cooled by cold gas. Using Eq. (1), the modulation of $\phi_\mathrm{c}$ ($\phi_\mathrm{c} \neq \Phi_\mathrm{c}$) can be compensated for when calculating $C_\mathrm{p}$ so that Regions 1 and 3 would not be distinguishable in Fig. 2(c). There is a Region 4 in Fig. 2(a) ($T < 239$ K) where no $h$ is recorded. This results from $\phi_\mathrm{c} \neq \Phi_\mathrm{c}$ [Fig. 2(b)], which extends the test duration required for finishing cooling until reaching 183 K. The time $t$ of record depends on the programmed thermal protocol and would be shortened due to $\phi_\mathrm{c} < \Phi_\mathrm{c}$. As shown in Fig. 2(d), at the final $t$ of 85 ms, the reference curve ends at 183 K, whereas the test curve ends at 239 K. Actually, at any moment during the test, the test curve is to the right of the reference curve, indicating a higher sample temperature than that of the reference temperature. Here, the slope of this curve denotes the inverse of $\phi_\mathrm{c}$.

Schawe *et al.*[25] have studied the $\phi_\mathrm{c}$ modulation of an Au-Ge eutectic alloy during fast cooling at a series of programmed $\Phi_\mathrm{c}$, where the four regions indicated in Fig. 2(a) can also be distinguished. They proposed that in Region 3, the system cooled in a ballistic manner. Ballistic cooling, on the other hand, is the last phase of achieving a temperature near absolute zero by allowing the cold-core temperature plummet as hot atoms ballistically escape. Region 3 would be properly described by Newton's law of cooling, which describes the cooling of a hot object in a cold environment when the primary mode of heat transfer is convection. A signature of Newtonian cooling is that $\phi_\mathrm{c}$ is proportional to the temperature difference between sample and environment, i.e., $T - T_\mathrm{e}$, which agrees well with our observation [Fig. 2(b)]. The reason why $\phi_\mathrm{c} < \Phi_\mathrm{c}$ is that $T - T_\mathrm{e}$ is no longer large enough to sustain the prescribed $\Phi_\mathrm{c}$.[29]

Figure 3(a) presents the cooling curve of the $Pd_{35}Ni_{45}P_{20}$ melt at a $\Phi_\mathrm{c}$ of 25,000 K·s$^{-1}$. Compared with Fig. 2(a), the $T$ range of Regions 1, 3, and 4 is widened, while that of Region 2 is narrowed. The expansions of Regions 1, 3, and 4 are all associated with the rising $\Phi_\mathrm{c}$ and consequently shorten Region 2. The effect of rising $\Phi_\mathrm{c}$ is significant, as Region 2 spans 620 K at 10,000 K·s$^{-1}$ but only spans 320 K at 25,000 K·s$^{-1}$. The narrowing of Region 2 with increasing $\Phi_\mathrm{c}$ comes mostly from Region 3 since the derivative of $\phi_\mathrm{c}$ with respect to $T$ remains unchanged [see Figs. 2(b) and 3(b)]. If we focus on the glass

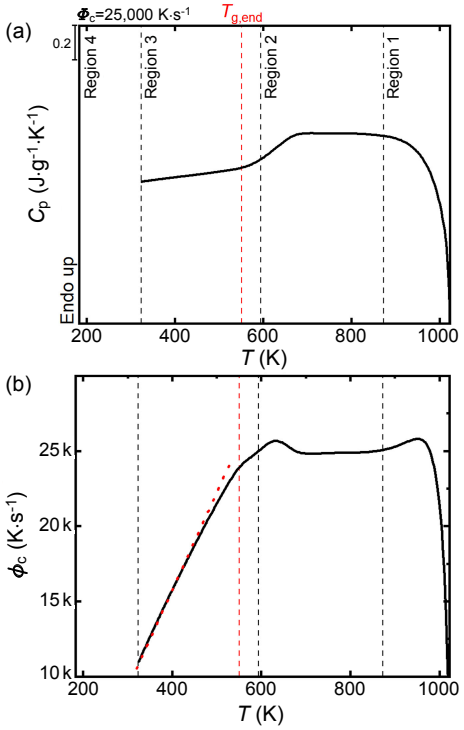


**Fig. 3.** Melt quenching of $Pd_{35}Ni_{45}P_{20}$ melt at a set cooling rate $\Phi_\mathrm{c}$ of 25,000 K·s$^{-1}$. (a) The cooling curve of specific heat capacity $C_\mathrm{p}$. $T_\mathrm{g,end}$ refers to the ending temperature of glass transition in cooling (as indicated by the red-dashed line). (b) The cooling rate $\phi_\mathrm{c}$ plotted against temperature $T$. The red-dotted line indicates a linear fit assuming Newtonian cooling.

transition in cooling at $\Phi_\mathrm{c}$, it takes place partially at a rate of 25,000 K·s$^{-1}$ but proceeds with decreasing $\phi_\mathrm{c}$ and ends at a lower $\phi_\mathrm{c}$. Calculating $C_\mathrm{p}$ by using $\phi_\mathrm{c}$ instead of $\Phi_\mathrm{c}$ reveals the complete process of glass transition. However, the glass transition is not ended at $\Phi_\mathrm{c}$ [Fig. 3(b)], so structural relaxation due to $\phi_\mathrm{c} < \Phi_\mathrm{c}$ needs to be considered.

From a test-designing point of view, we need to estimate the upper and lower temperatures of Region 2 ($T_\mathrm{u}$ and $T_\mathrm{l}$) to find the maximum $\Phi_\mathrm{c}$ that enables observation of a complete glass transition on the cooling curve. We found an empirical equation for $T_\mathrm{u}$, that is

$$T_\mathrm{u} = T_\mathrm{q} - a\Phi_\mathrm{c} - b, \tag{4}$$

where $a$ and $b$ are fitting parameters. For the 230 ng $Pd_{35}Ni_{45}P_{20}$ specimen, $a = 1.40 \pm 0.03$ ms, and $b = 6.8 \pm 0.5$ K. The $a$ value is close to thermal lag that is usually estimated by compensating the $\phi_\mathrm{c}$-shifted $T_\mathrm{m}$ from the measurement.[30] Thus, at the technical limit of $\Phi_\mathrm{c} = 40,000$ K·s$^{-1}$, $T_\mathrm{u}$ is about $0.93T_\mathrm{q}$. The MG formers have their $T_\mathrm{q} < 0.6T_\mathrm{m}$ ($T_\mathrm{m}$: the melting temperature).[31] Because $T_\mathrm{q}$ is set higher than $T_\mathrm{m}$ for melt quenching, $T_\mathrm{g} < 0.6T_\mathrm{q}$, and hence $T_\mathrm{g} < 0.6T_\mathrm{u}$. In other words, $T_\mathrm{u}$ would not hide glass transition in cooling, even if the FDSC test is performed at the highest $\Phi_\mathrm{c}$. However, $T_\mathrm{u}$ might affect crystallization in cooling if the "nose" temperature of crystallization in the continuous-cooling-temperature diagram approaches $T_\mathrm{m}$ and hence close to $T_\mathrm{u}$. In this case, $T_\mathrm{q}$ should be set much larger than $T_\mathrm{m}$ in order to let $\phi_\mathrm{c}$

reach $\Phi_c$ before undercooling.

The $T_l$ can be calculated from the Newton's law of cooling by

$$T_l = T_e + \frac{1-c}{k}\Phi_c, \tag{5}$$

where $c$ is a parameter compensating the delay in Region 4, and $k$ is a $\phi_c$-independent constant depending on both material properties and environment. For the 230 ng $Pd_{35}Ni_{45}P_{20}$ specimen, $k$ is $66 \pm 12\,s^{-1}$, and at $\Phi_c = 25,000\,K{\cdot}s^{-1}$, $c$ is $1 \times 10^{-3}$, which can be neglected for $T_l$ estimation. Since glass transition happens on the lower-$T$ part of Region 2, the highest cooling-rate applicable to observe glass transition in cooling ($\Phi'_c$) can be estimated by setting $T_l = T_g$ in Eq. (5). Neglecting $c$,

$$\Phi'_c = k(T_g - T_e). \tag{6}$$

For the $Pd_{35}Ni_{45}P_{20}$ (230 ng) whose $T_g$ is 573 K at $\phi_h = 20\,K{\cdot}min^{-1}$ in DSC, $\Phi'_c$ is around $25{,}740\,K{\cdot}s^{-1}$ when $T_e$ equals 183 K.

According to Eq. (4), increasing $\Phi'_c$ can be achieved by increasing $k$ or lowering $T_e$. We found that $k$ is sensitive to $m$. Figure 4(a) shows the cooling curves of two $Au_{42.3}Ag_{5.6}Pd_{2.4}Cu_{27.5}Si_{22.2}$ MG-forming melts quenched from a $T_q$ of 973 K at a $\Phi_c$ of $6{,}000\,K{\cdot}s^{-1}$. When $m$ of the specimen is 420 ng, $T_l$ of its Region 2 is 387 K, interrupting the glass transition in cooling as the ending temperature of glass transition $T_{g,end}$ is smaller than $T_l$. However, after reducing $m$ to 290 ng, $T_l$ shifts by −10 K and equals to $T_{g,end}$. From Fig. 4(b), it is clear that $k$ in Region 3 increases with the decreasing $m$. Therefore, a small-mass specimen is always preferred for fast cooling in FDSC.

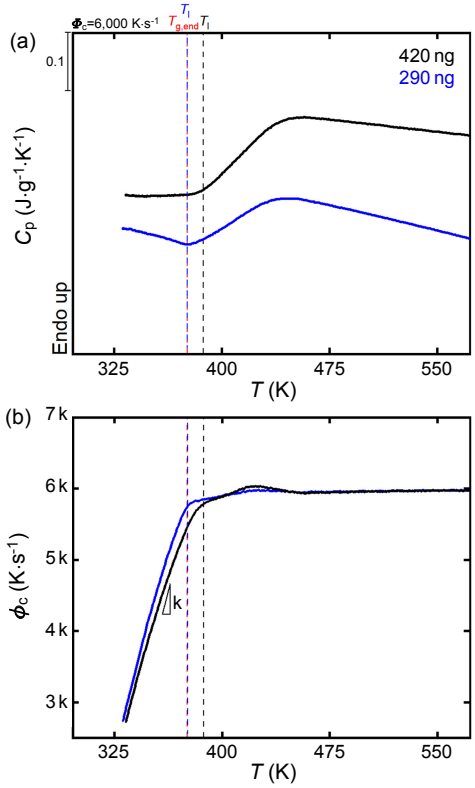


**Fig. 4.** Melt quenching of an $Au_{42.3}Ag_{5.6}Pd_{2.4}Cu_{27.5}Si_{22.2}$ MG. (a) The cooling curve of specific heat capacity $C_p$ at masses of 420 ng (black curve) and 290 ng (blue curve), respectively. The set cooling rate $\Phi_c$ is $6{,}000\,K{\cdot}s^{-1}$, and the environmental temperature $T_e$ is 300 K. The ending point of the glass transition in cooling, $T_{g,end}$, is indicated by the red-dashed line. The lower-boundary temperature of Region 2, $T_l$, is marked by the black-dashed line for the 420 ng (and blue-dashed line for the 290 ng). (b) The cooling rate $\phi_c$ plotted against temperature $T$. The slope $k$ relevant to Newtonian cooling is indicated by the triangle.

An alternative option for raising $\Phi'_c$ is to decrease $T_e$ from the gas coolant. The gas is cooled by a cold plate containing microchannels flowing with the fluid coolant. Using liquid nitrogen instead of water, we lowered $T_e$ from 300 K to 223 K for the $Au_{42.3}Ag_{5.6}Pd_{2.4}Cu_{27.5}Si_{22.2}$. The benefits are obvious. Figure 5(a) shows the cooling curves obtained at a $\Phi_c$ of $8{,}000\,K{\cdot}s^{-1}$. At $T_e$ = 300 K, the glass transition is partially revealed on the cooling curve; at $T_e$ = 223 K, Region 2 covers the complete process of glass transition. If we compare the fictive temperature ($T_f$), as calculated from the reheating curve using the area-equivalent method proposed by Moynihan *et al.*,[32] we find that $T_f$ = 428.9 K at $T_e$ = 223 K, which is 3.8 K higher than $T_f$ = 425.1 K at $T_e$ = 300 K [Fig. 5(a)].

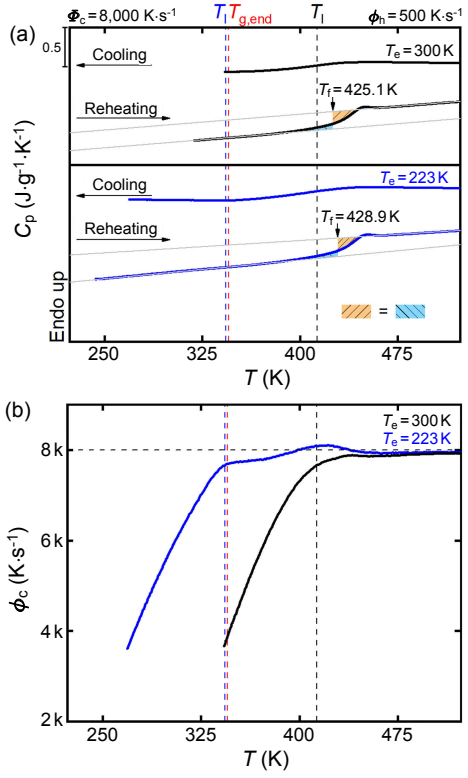


**Fig. 5.** Melt quenching of $Au_{42.3}Ag_{5.6}Pd_{2.4}Cu_{27.5}Si_{22.2}$ MGs (420 ng). (a) The cooling and reheating curves of specific heat capacity $C_p$ at environment temperatures $T_e$ of 300 K (black curve) and 223 K (blue curve), respectively. The programmed cooling-rate $\Phi_c$ is $8{,}000\,K{\cdot}s^{-1}$, and the heating rate is $500\,K{\cdot}s^{-1}$. The end of the glass transition in cooling $T_{g,end}$ is indicated by the red-dashed line. The lower boundary temperature of Region 2 ($T_l$) is marked by the black-dashed line for the $T_e$ = 300 K (and blue-dashed line for the $T_e$ = 223 K). Grey curves are baselines for liquid and glass states. The fictive temperature $T_f$ is determined by the equal-area principle. (b) The cooling rate $\phi_c$ plotted against temperature $T$.

Actually, this latter value of $T_f$ corresponds to $\Phi_c = 4,600\,\mathrm{K{\cdot}s^{-1}}$ based on our estimation assuming that $T_f$ varies linearly with $\Phi_c$, indicating structural relaxation during the glass transition in cooling. From Fig. 5(b), it can be seen that $T_{g,end}$ intersects a $\phi_c$ of $8{,}000\,\mathrm{K{\cdot}s^{-1}}$ for $T_e = 223\,\mathrm{K}$ but intersects a $\phi_c$ of $3{,}600\,\mathrm{K{\cdot}s^{-1}}$ for $T_e = 300\,\mathrm{K}$. It is then not surprising to witness that $T_f$ lowers when cooled at $T_e = 300\,\mathrm{K}$ because $\phi_c < \Phi_c$.

In conclusion, we examine the cooling curves of two melt-quenched MG formers. We showed how the cooling process can be divided into four distinct regions. When we compared the sample's cooling rate with the programmed one, we saw that from Regions 1 to 4, it first catches up, then equals, decreases, and eventually disappears. In order to extend the investigation window of Region 2 where the sample is at the set cooling rate, we use either empirical or theoretical methods to establish the upper boundary and lower boundary temperatures. Lowering sample mass and decreasing the environment temperature are found to be helpful in increasing the cooling rate while simultaneously witnessing a complete glass transition during cooling. Improper selection of these parameters can cause structural relaxation during glass transition due to a decreasing cooling rate, as confirmed by the fictive temperature determined from the reheating curves.

*Acknowledgements.* This work was supported by the National Natural Science Foundation of China (Grant Nos. 92580120 and 52471188). The AI-driven experiments, simulations and model training were performed on the robotic AI-Scientist platform of Chinese Academy of Sciences.

# References

[1] Rangarajan S, Schiffres S N, and Sammakia B 2023 *Engineering* **26** 185
[2] Luo X, Sun Y H, and Wang W H 2025 *Sci. China Phys. Mech. Astron.* **68** 266102
[3] Ashby M F and Greer A L 2006 *Scripta Mater.* **54** 321
[4] Li X, Zhou J, Shen L, Sun B, Bai H, and Wang W 2022 *Adv. Mater.* **35** 2205863
[5] Lan S, Wu Z D, and Wang X L 2017 *Chin. Phys. B* **26** 017104
[6] Zhang S, Wang W H, and Guan P F 2021 *Chin. Phys. Lett.* **38** 016802
[7] Li Z J, Zhao R Z, Wang Y T, Chen Z M, Tu W K, Zhang Y Q, Bo H, Liu Y D, and Wang L M 2016 *Chin. Phys. Lett.* **33** 046401
[8] Qin B, Xu H, Tan X H, and Meng T 2009 *Chin. Phys. Lett.* **26** 057503
[9] Cao C D, Gong S L, Guo J B, Song R B, Sun Z B, Yang S, and Wang W M 2012 *Chin. Phys. B* **21** 086102
[10] Bokas G B, Zhao L, Morgan D, and Szlufarska I 2017 *J. Alloys Compd.* **728** 1110
[11] Kim Y J, Busch R, Johnson W L, Rulison A J, and Rhim W K 1996 *Appl. Phys. Lett.* **68** 1057
[12] Zhang H R, Yang Q, Fang Z L, Zhang W X, Yin Z, Zeng M H, and Yu H B 2025 *Sci. China Phys. Mech. Astron.* **68** 266103
[13] Liu M, Wang Z, Ding Y, Meng S, and Hu L 2025 *Sci. China Phys. Mech. Astron.* **68** 266104
[14] Shen J, Lu Z, Wang J Q, Lan S, Zhang F, Hirata A, Chen M W, Wang X L, Wen P, Sun Y H, Bai H Y, and Wang W H 2020 *J. Phys. Chem. Lett.* **11** 6718
[15] Shen J, Sun Y H, Orava J, Bai H Y, and Wang W H 2022 *Acta Mater.* **225** 117588
[16] Shen J, Zhang H P, Chen Z Q, Ouyang L F, Wang F R, Lu Z, Li M Z, Sun Y H, Bai H Y, and Wang W H 2023 *Acta Mater.* **244** 118554
[17] Cheng Q, Sun Y H, and Wang W H 2023 *Acta Phys. Sin.* **73** 078101 (in Chinese)
[18] Cheng Q, Sun Y H, Orava J, and Wang W H 2025 *Acta Mater.* **289** 120940
[19] Cheng Q, Han X, Kaban I, Soldatov I, Wang W H, Sun Y H, and Orava J 2020 *Scr. Mater.* **183** 61
[20] Cheng Q, Sun Y H, Orava J, Bai H Y, and Wang W H 2022 *Acta Mater.* **230** 117834
[21] Cheng Q, Sun Y H, and Wang W H 2025 *Sci. China Phys. Mech. Astron.* **68** 266105
[22] Cheng Q, Wang P F, Jiang H Y, Gu L, Orava J, Sun Y H, Bai H Y, and Wang W H 2021 *Phys. Rev. B* **103** L100203
[23] Cheng Q, Sun Y H, Orava J, and Wang W H 2023 *Mater. Today Phys.* **31** 101004
[24] Schawe J E K 2015 *Thermochim. Acta.* **603** 128
[25] Schawe J E K, Willinger M G, Stanko S T, Stoica M, and Löffler J F 2025 *Mater. Today Adv.* **27** 100597
[26] Ouyang L F, Shen J, Huang Y, Sun Y H, Bai H Y, and Wang W H 2023 *J. Appl. Phys.* **133** 085105
[27] Yamasaki M, Kagao S, and Kawamura Y 2005 *Scripta Mater.* **53** 63
[28] Pryadun V V, Louzguine-Luzgin D V, Shvanskaya L V, and Vasiliev A N 2015 *JETP Lett.* **101** 465
[29] Schick C and Mathot V 2016 *Fast Scanning Calorimetry* (Switzerland: Springer Nature) p. 330
[30] Pogatscher S, Uggowitzer P J, and Löffler J F 2014 *Appl. Phys. Lett.* **104** 251908
[31] Turnbull D 1969 *Contemp. Phys.* **10** 473
[32] Moynihan C T, Easteal A J, Debolt M A, and Tucker J 1976 *J. Am. Ceram. Soc.* **59** 12